nature COMMUNICATIONS

ARTICLE

Received 13 Mar 2015 | Accepted 13 May 2015 | Published 3 Jul 2015

DOI: 10.1038/ncomms8493 OPEN

Edge-terminated molybdenum disulfide with a 9.4-Å interlayer spacing for electrochemical hydrogen production

Min-Rui Gao[1], Maria K.Y. Chan[1] & Yugang Sun[1]

Layered molybdenum disulfide has demonstrated great promise as a low-cost alternative to platinum-based catalysts for electrochemical hydrogen production from water. Research effort on this material has focused mainly on synthesizing highly nanostructured molybdenum disulfide that allows the exposure of a large fraction of active edge sites. Here we report a promising microwave-assisted strategy for the synthesis of narrow molybdenum disulfide nanosheets with edge-terminated structure and a significantly expanded interlayer spacing, which exhibit striking kinetic metrics with onset potential of -103 mV, Tafel slope of 49 mV per decade and exchange current density of 9.62×10^{-3} mA cm^{-2}, performing among the best of current molybdenum disulfide catalysts. Besides benefits from the edge-terminated structure, the expanded interlayer distance with modified electronic structure is also responsible for the observed catalytic improvement, which suggests a potential way to design newly advanced molybdenum disulfide catalysts through modulating the interlayer distance.

[1] Center for Nanoscale Materials, Argonne National Laboratory, 9700 South Cass Avenue, Argonne, Illinois 60439, USA. Correspondence and requests for materials should be addressed to Y.S. (email: ygsun@anl.gov).

The blueprint of 'hydrogen (H_2) economy' is to store energy from renewable sources, such as sunlight or wind, into the chemical bond of H_2 via electrolysis of water, which then can be released through the reverse reaction in fuel cells on demand[1]. However, the scalable production of H_2 from water significantly depends on the efficiency of electrocatalytic materials. Ideal electrocatalysts must be, stable and capable of reducing water rapidly at potentials close to its thermodynamic value ($2H^+ + 2e^- \rightarrow H_2$; $0 - 0.059 \times$ pH, V versus normal H_2 electorde at 298 K)[2,3]. Although platinum (Pt) and its alloys can catalyse H_2 evolution reaction (HER) at potentials slightly below the thermodynamic potential for the H^+/H_2 couple[2–4], the high cost and scarcity of Pt pose tremendous limitation to widespread adoption. Therefore, the critical determinant of the energy storage in electrolytic systems is to develop robust and efficient alternative catalysts that are cheap and Earth abundant.

Remarkable advances have been made recently regarding the use of chalcogenides of cobalt[5–9], nickel[8,10], molybdenum[9,11–19] and tungsten[15,20,21] as promising noble metal-free catalysts for HER. Among these materials, molybdenum disulfide (MoS_2), a widely used industrial catalyst for hydrodesulfurization of petroleum[22], has received special attention and the catalytic active sites were identified theoretically[23] and experimentally[24]. Similar to many inorganic solids, the HER activity of MoS_2 is localized to the rare edge surfaces, whereas the (0001) basal planes are relatively inactive[23–25]. Motivated by this understanding, intense research efforts have been focused on developing highly nanostructured MoS_2 to maximize the number of exposed edge sites, including crystalline[26–29] and amorphous materials[12,15,30,31], metallic 1T polymorph[9,32], vertically aligned structures[33,34] and molecular mimics[25]. Other strategies to improve HER performance include incorporating MoS_2 with conductive materials by taking advantage of synergetic coupling effects[34–38] or doping first-row transition metal ions (for example, Fe, Co and Ni) into MoS_2 to optimize its catalytic sites at S-edges[26,39]. Despite striking achievements, many practical challenges still remain to improve the activity and stability of MoS_2-based catalysts.

Here, we report a class of colloidal MoS_2 nanostructure with edge-terminated and interlayer-expanded (ET&IE) features that exhibits high activity and stability towards HER in acidic water. Its fast kinetic metrics (including onset potential of -103 mV and the Tafel slope of 49 mV per decade) demonstrate superior electrocatalytic activity relative to the reported MoS_2-only catalysts. In addition to the benefit of edge-terminated structure, the expansion of interlayers can further modify electronic structures and electrical conductivity of MoS_2 edge sites, leading to improved performance. This study hints at the promise of cheap and efficient HER electrocatalysts by modulating interlayer distance in two-dimensional atomic-layered materials.

Results

Microwave-assisted synthesis of ET&IE MoS_2. The ET&IE MoS_2 were synthesized through reduction of $(NH_4)_2MoS_4$ in *N*,*N*-dimethylformamide (DMF) with the assistance of microwave heating. Compared with conventional heating methods, microwave-assisted synthesis is a greener strategy with high-level thermal management and dramatically reduced reaction time and therefore new nanostructured materials are likely to be achieved[40]. Reaction at 240 °C for 2 h results in a yield of ~93% of ET&IE MoS_2, demonstrating the rapid and efficient microwave chemistry. A schematic overview of the synthesis procedure is shown in Fig. 1 and the details are described in the Methods. The morphology and microstructure of MoS_2 prepared at different

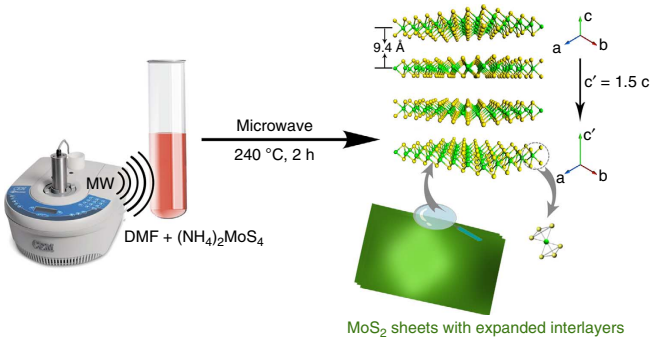

Figure 1 | Schematic illustration of the synthesis of ET&IE MoS_2. The *c* axis of the as-synthesized MoS_2 shows about 1.5 × expansion as compared with that of standard 2H-MoS_2 phase. Green and yellow balls indicate Mo and S atoms, respectively.

temperatures was studied by transmission electron microscopy (TEM) (Fig. 2a–c) and high-resolution TEM (HRTEM) (Fig. 2d–f). Reaction at low temperature (for example, 190 °C) forms reticulated network of amorphous materials (Fig. 2a), where some tiny MoS_2-layered crystals appear (Fig. 2d), indicating the formation of crystalline nuclei from the amorphous matrix. Increasing reaction temperature results in the formation and growth of crystalline nuclei into larger MoS_2 nanocrystals via consumption of the amorphous materials. For example, MoS_2 synthesized at 240 °C exhibits a sheet-like morphology with sizes of tens of nanometres (Fig. 2b). HRTEM image in Fig. 2e clearly shows the resolved S–Mo–S layers with a curved stripe-like feature (Supplementary Fig. 1) and the layer-to-layer spacing is about 9.4 Å. Further increasing temperature to 260 °C produces three-dimensional flower-like MoS_2 with better crystallinity (Fig. 2c and inset). HRTEM image of a typical MoS_2 flower reveals that it is built from interlaced crystalline MoS_2 nanosheets (Fig. 2f).

Figure 2g presents the X-ray diffraction patterns of these samples, which are significantly different from that of bulk 2H–MoS_2 (JCPDS 77-1,716; Supplementary Fig. 2). Two new peaks with diploid relationship appears at low-angle region correspond to (001) and (002) reflections with *d* spacings of 9.4 and 4.7 Å, respectively. In comparison to the *d* spacing of 6.15 Å for pristine 2H–MoS_2, the expanded interlayers of our samples is likely due to the intercalation of oxidized DMF species into two S–Mo–S layers (Supplementary Fig. 3). The asymmetric nature of the reflection at $2\theta \approx 32.7°$ revealed the presence of stacking faults[41] among MoS_2 layers as a result of *a*–*b* plane gliding caused by intercalated DMF species. A recent work also reported a large interlayer spacing of 9.5 Å in hydrothermally prepared MoS_2, which however was ascribed to oxygen incorporation[29]. Unlike the product formed at 260 °C, the barely recognizable diffraction peaks of other two samples indicate the low crystallinity, which is consistent with their selected-area electron diffraction (SAED) patterns. Particularly, the greatly broad first peak for 240 °C sample was the result of its curly and crossed edge-terminated structure (Fig. 2e). The calculated X-ray diffraction pattern using an interlayer spacing of 9.4 Å along the *c* axis was found to agree well with experimentally collected patterns (Fig. 2g). Energy-dispersive X-ray spectra showed that the as-synthesized samples are mainly composed of Mo and S (Supplementary Fig. 4). Raman spectra in Fig. 2h exhibited two distinct peaks at 379.2 cm^{-1} and 402.7 cm^{-1}, which correspond to the in-plane Mo–S phonon mode (E^1_{2g}) and the out-of-plane Mo–S mode (A_{1g}) of typical MoS_2-layered structure, respectively[33,37]. The relative intensities of A_{1g}/E^1_{2g} provide texture information on the surface of deposited MoS_2 films and the largest ratio of 2.02 for 240 °C

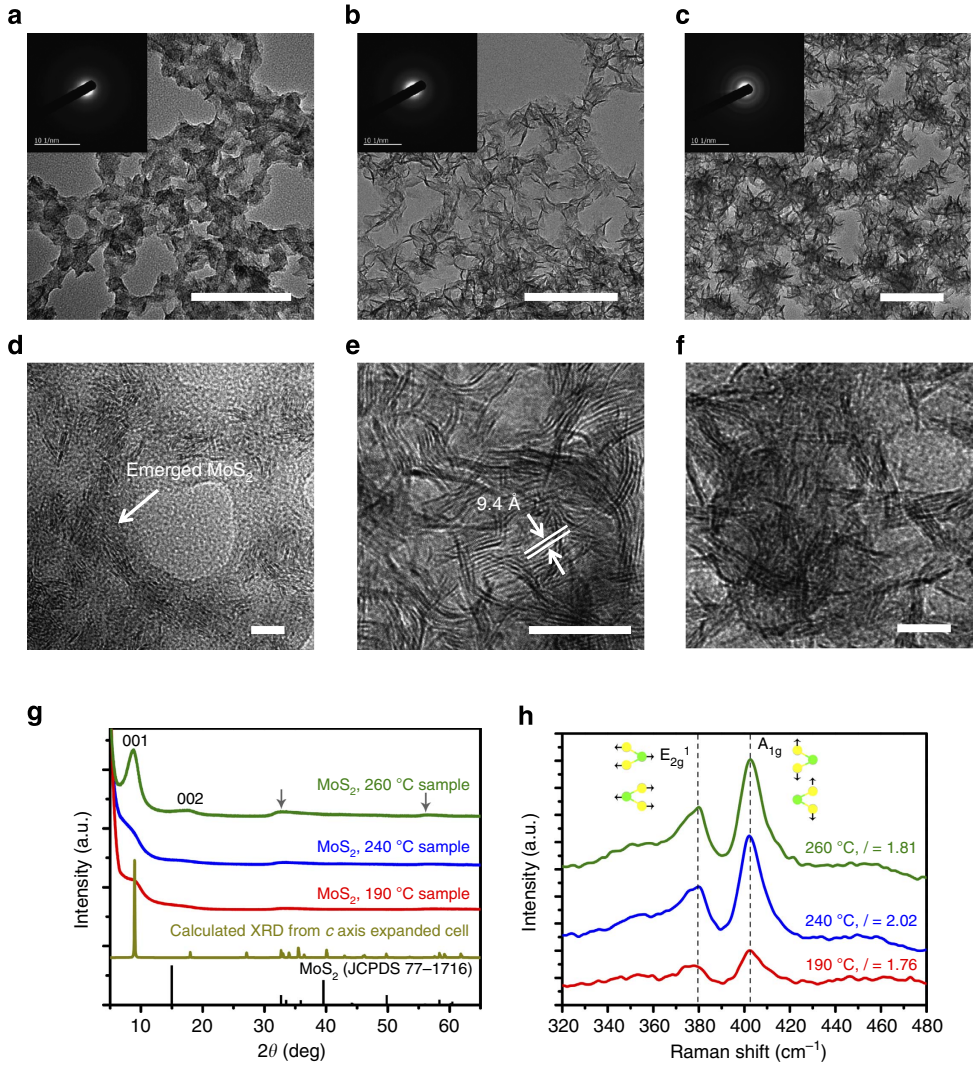

Figure 2 | Characterization of the MoS_2 nanosheets. (**a**–**c**) TEM images of MoS_2 nanostructures synthesized at 190 °C (**a**), 240 °C (**b**) and 260 °C (**c**). Scale bars, 100 nm. The insets in (**a**–**c**) show corresponding SAED patterns, respectively. (**d**–**f**) HRTEM images of MoS_2 nanostructures synthesized at 190 °C (**d**), 240 °C (**e**) and 260 °C (**f**). Scale bars, 10 nm. (**g**) X-ray diffraction patterns of MoS_2 nanostructures synthesized at different temperatures. The calculated pattern from *c* axis expanded MoS_2 cell and the standard pattern of the pristine 2H-MoS_2 (JCPDS 77-1,716) are shown as reference. (**h**) Raman spectra of the different MoS_2 products. The larger relative intensity of A_{1g}/E^1_{2g} for 240 °C sample ($I = 2.02$) suggests its edge-terminated structure.

sample suggests that it favours the vibration of A_{1g} mode and thus the best edge-terminated structure[33,37], which is consistent with the TEM observations (Fig. 2a–f). The phase and morphology evolutions of ET&IE MoS_2 were also studied by time-dependent reactions at 240 °C and the results are presented in Supplementary Figs 5 and 6.

Electrocatalytic HER activity. The electrocatalytic properties of ET&IE MoS_2 for evolving H_2 were evaluated in Ar-saturated 0.5 M H_2SO_4 electrolyte and compared with state-of-the-art Pt/C catalyst. The ohmic potential drop (iR) losses from the solution resistance were corrected. The electrodes were kept rotating at 1,600 r.p.m throughout the measurements in order to remove *in situ* produced H_2 bubbles. Figure 3a compares the current densities achieved within a cathodic potential window for the glassy carbon electrodes modified with different catalysts. The featureless polarization curve for bare glassy carbon guarantees a minimal background. Scanning cathodically reveals that the onset potential of H_2 evolution occurs at approximately -0.10 V versus reversible hydrogen electrode (RHE) for the MoS_2 synthesized at 240 °C, beyond which a sharp increase in catalytic reduction current emerges (Fig. 3a). The optimum catalyst loading was determined to be 0.28 mg cm^{-2} (Supplementary Fig. 7). In contrast, MoS_2 prepared at 190 °C and 260 °C mediate hydrogen evolution at larger overpotential (η) of 0.15 and 0.12 V, respectively, while bulk MoS_2 offers negligible H_2-evolving activity. The superior activity of the MoS_2 synthesized at 240 °C is believed to originate from both its edge-terminated and interlayer-expanded structure. The dependence of the logarithmic current density on η ($\log j$–η) was plotted to probe the HER kinetics. Figure 3b shows that a sharp increase in current density appeared once the onset potential was reached. The linear relationship of $\log j$ and η delivers useful kinetic metrics of above catalysts, namely the Tafel slope. The Tafel slope of 49 mV per decade was measured for the MoS_2 synthesized at 240 °C, which is smaller than those of other catalysts except for the state-of-the-art Pt/C catalyst (Fig. 3b). This Tafel slope is comparable to or smaller than that of other MoS_2-only HER catalysts (Supplementary Table 1) and even many MoS_2-based hybrid catalysts (Supplementary Table 2) reported in literature, indicating the efficient kinetics of H_2 evolution catalysed by the MoS_2 synthesized at 240 °C. The η

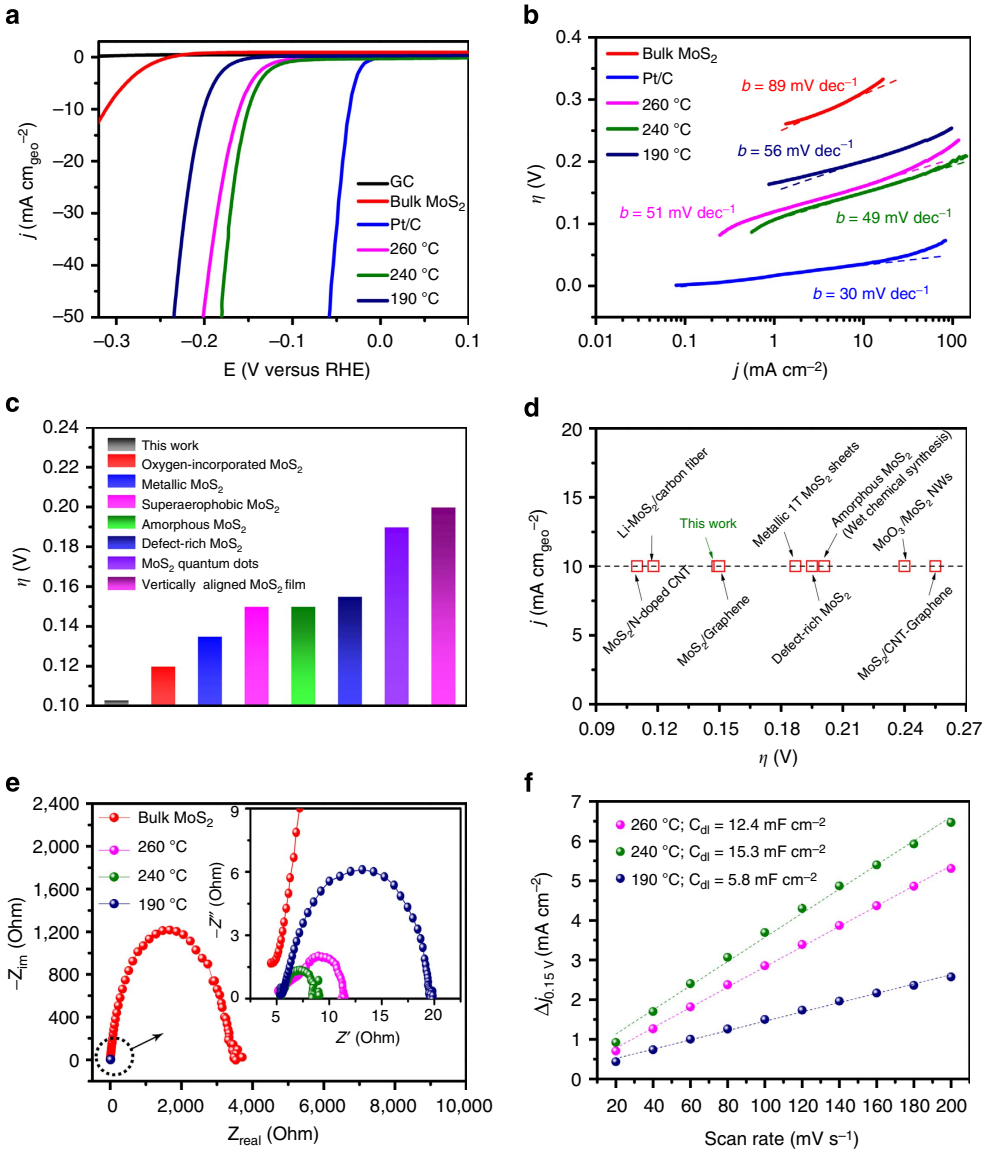

Figure 3 | Electrocatalytic hydrogen evolution of the catalysts. (**a**) Polarization curves for HER on bare glassy carbon electrode and modified glassy carbon electrodes comprising MoS_2 nanosheets synthesized from different temperatures, bulk MoS_2 and a high quality commercial Pt/C catalyst. Catalyst loading is 0.28 mg cm^{-2} for all samples. Sweep rate: 5 mV s^{-1}. (**b**) Tafel plots for the various catalysts derived from **a**. (**c**) Comparison of η required to initiate HER on various MoS_2-only catalysts, including oxygen-incorporated MoS_2 (ref. 26), metallic MoS_2 (ref. 29), superaerophobic MoS_2 (ref. 17), amorphous MoS_2 (ref. 28), defect-rich MoS_2 (ref. 25), MoS_2 quantum dots[18] and vertically aligned MoS_2 film[30]. (**d**) Comparison of η required to generate a current density of 10 mA cm$_{geo}^{-2}$ on various MoS_2-based catalysts, including MoS_2/N-doped carbon nanotube (CNT)[49], Li-MoS_2/carbon fibre[37], MoS_2/graphene[33], metallic MoS_2 (ref. 29), defect-rich MoS_2 (ref. 25), amorphous MoS_2 (ref. 28), MoO_3/MoS_2 NWs[19] and MoS_2/CNT-graphene[38]. (**e**) EIS Nyquist plots of bulk MoS_2 and synthesized MoS_2 nanosheets. Inset shows Nyquist plots at high-frequency range. Z' is the real impendence and Z'' is the imaginary impedance. (**f**) Plots showing the extraction of the C_{dl} for different MoS_2 electrodes. All the measurements were performed in Ar-saturated 0.5 M H_2SO_4 (pH ~ 0) and the reported data were iR compensated.

required for starting HER on various MoS_2-only catalysts was compared in Fig. 3c, where ET&IE MoS_2 shows a 20–100 mV decrease in η relative to that of documented MoS_2. The fast HER kinetics also enabled this ET&IE MoS_2 catalyst to reach a high current density of 10 mA cm^{-2} at η as low as 0.149 V, outperforming most of the MoS_2-based HER catalysts (Fig. 3d, Supplementary Tables 1 and 2). Exchange current density (j_0), the most inherent measure of HER activity, was carefully determined to evaluate the quality of ET&IE MoS_2 (Supplementary Fig. 8). The j_0 of 9.62×10^{-3} mA cm^{-2} for 240 °C sample surpasses the values of 7.59×10^{-4} mA cm^{-2} for 190 °C sample and 2.46×10^{-3} mA cm^{-2} for 260 °C sample, as well as the j_0 values reported for MoS_2-only HER catalysts (Supplementary Table 1). Moreover, the turnover frequency of H_2 molecules evolved per second (s^{-1}) for ET&IE MoS_2 was determined to be 1.14 s^{-1} at η of 200 mV, comparing favourably with the reported MoS_2-only and even some MoS_2-based hybrid catalysts (Supplementary Table 3 and Supplementary Note 1). These results highlight the exceptional H_2-evolving efficiency of this new ET&IE MoS_2.

We also applied electrochemical impedance spectroscopy (EIS) technique to provide further insight into the electrode kinetics under HER process (that is, adding a η of 0.2 V). The Nyquist plots (Fig. 3e and inset) show that ET&IE MoS_2 synthesized at 240 °C has the smallest charge transfer resistance (R_{ct}) of only 3.13 Ω, indicating the ultrafast Faradaic process and thus a superior HER kinetics. We attribute this measured small R_{ct} to its

synergetic ET&IE structure. The edge-terminated feature can ensure an isotropic electron transport from glassy carbon substrate to MoS_2 edges and significantly decrease the resistance for traversed layers. In addition, the expanded interlayer distance can bring beneficial structural and electronic modulations (which will be discussed below), enabling each MoS_2 layer to resemble more closely to a monolayer structure and a better overall conductivity of our ET&IE MoS_2. The double-layer capacitance (C_{dl}), which is proportional to the effective electrochemically active surface area[27,32], was further measured to probe the advantage of the ET&IE structure (Fig. 3f). The observed large C_{dl} of 15.3 mF cm^{-2} for 240 °C sample indicated its high exposure of active edge sites, comparing favourably with other studied catalysts (Fig. 3f, Supplementary Fig. 9) and thus the improved HER activity. HER performance of the MoS_2 nanostructures synthesized at 240 °C for different reaction times was compared and the results are presented in Supplementary Figs 10 and 11.

Material stability of ET&IE MoS_2. The long-term stability of ET&IE MoS_2 and associated ability to continuously catalyse the generation of H_2 was examined using chronoamperometry ($j \sim t$). This quasi-electrolysis process was conducted at a constant η of 200 mV in 0.5 M H_2SO_4 (Fig. 4a). Remarkably, the H_2 evolution can proceed at a sustained current density of -28 mA cm^{-2} even over 65 h of continuous operation, suggesting the ultrahigh stability of the ET&IE MoS_2 catalyst. The striking stability was further proved by a long-term cyclic voltammetry cycling test operating in the same electrolyte. Figure 4b shows that, after 3,000 cyclic voltammetry cycles, only negligible decay was observed in high current density region, where the massive H_2 bubbles generated at the electrode surface raise the mass transport resistance for the HER. Moreover, this new MoS_2 demonstrates good chemical stability with no obvious degradation of HER activity after storing it under lab environment for 3 months (Supplementary Fig. 12). Digital photos (Fig. 4c) taken from the ET&IE MoS_2-coated fluorine-doped tin oxide (FTO) show vigorous effervescence maintained with no decay even after 5 h of continuous operation while clean FTO is inert (Supplementary Fig. 13). The substantial long-term stability and chemical stability of ET&IE MoS_2 suggest the great promise of using this catalyst to fabricate cost-effective and efficient H_2 evolution electrode in viable water electrolysis systems.

HER enhancement mechanism. An understanding of intrinsic reasons for the remarkable HER property of ET&IE MoS_2 will be helpful for future HER catalyst design. It is agreed that for a highly active HER catalyst the Gibbs free energy of adsorbed hydrogen (ΔG_H) is close to thermoneutral (that is, $\Delta G_H \approx 0$)[4,23,26]. Deviating from this value will make the hydrogen either form a strong bond or not bind efficiently to the catalyst, leading to inefficient hydrogen release and proton–electron transfer and therefore decreased catalytic activity. Recent density functional theory (DFT) calculations revealed that MoS_2 has a ΔG_H of 0.08 eV at the Mo edges and should be a good HER catalyst[23]. This prediction was later experimentally verified by the finding that MoS_2 edge sites are highly HER active while its basal planes are inert[24]. Here, our microwave-synthesized MoS_2 preferentially has a high ratio of catalytically active edge sites relative to basal sites due to its highly curved sheet-like structure (Fig. 2b,e and Supplementary Fig. 1), which provides one reason for its striking HER activity.

The superior j_0 (9.62×10^{-3} mA cm^{-2}) of the ET&IE MoS_2 relative to that of documented MoS_2 (Supplementary Table 1) prompted us to further consider another underlying enhancement mechanism in this material. Previous reports demonstrated that the electronic structure of MoS_2 can be modified to optimize

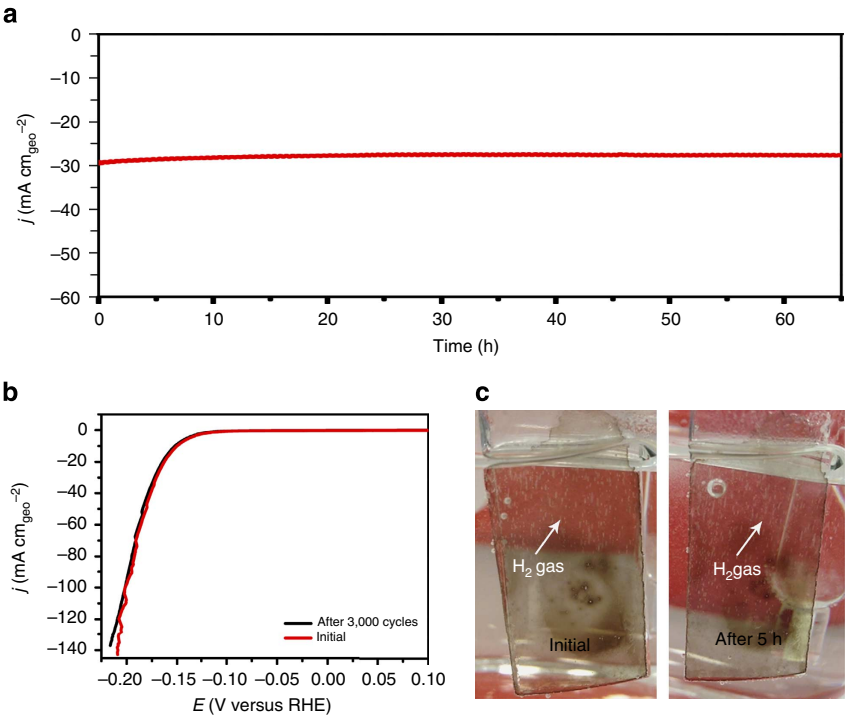

Figure 4 | HER stability of ET&IE MoS_2. (**a**) Chronoamperometric responses ($j \sim t$) recorded from synthesized ET&IE MoS_2 at a constant overpotential of 200 mV (no iR compensation). (**b**) Polarization curves recorded from ET&IE MoS_2 with a sweep rate of 5 mV s^{-1} before and after 3,000 potential cycles between -0.3 and 0.3 V versus RHE at a sweep rate of 200 mV s^{-1} (with iR compensation). (**c**) Digital photos show the H_2 bubbles on ET&IE MoS_2-modified FTO before and after 5 h of operation (MoS_2 loading: ~22.1 μg cm^{-2}). All the measurements were performed in Ar-saturated 0.5 M H_2SO_4 (pH ~ 0).

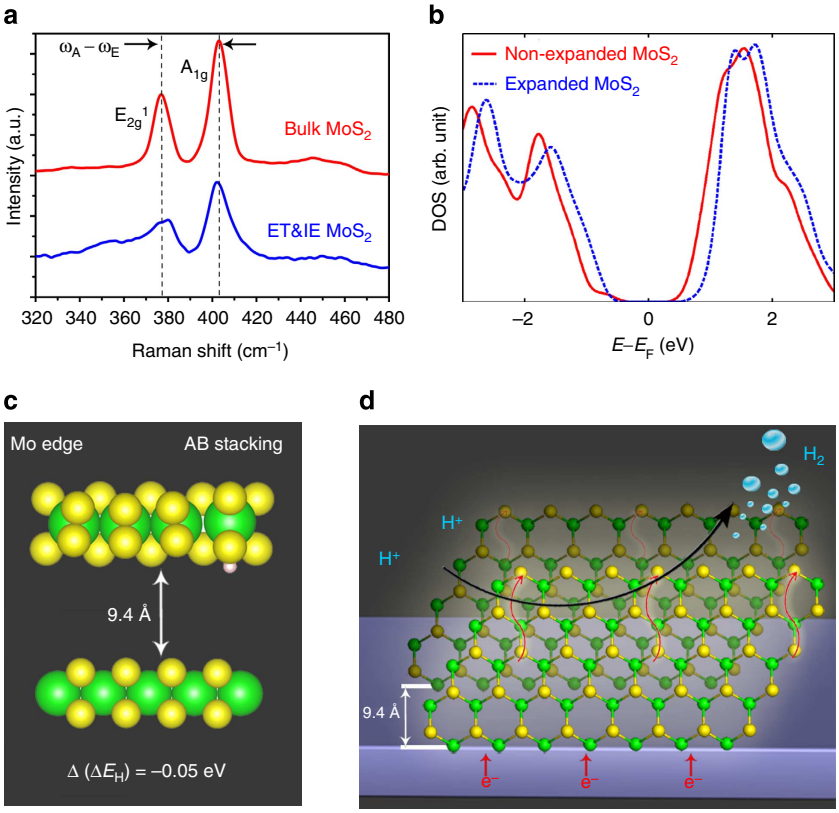

Figure 5 | HER enhancement mechanism. (**a**) Raman spectra of bulk MoS_2 and ET&IE MoS_2. (**b**) The projected DOS on non-expanded MoS_2 and interlayer-expanded MoS_2. (**c**) DFT calculation of the change in hydrogen adsorption energy ($\Delta(\Delta E_H)$) between the ET&IE MoS_2 and non-expanded MoS_2. (**d**) Schematic representation of the edge-terminated MoS_2 on glassy carbon electrode for HER, where the interlayer spacing is 9.4 Å. Green, yellow and white balls indicate Mo, S and H atoms, respectively.

ΔG_H[24,26,39,42]. For example, Co incorporation at S-edges can reduce the ΔG_H from 0.18 to 0.1 eV and offer faster proton adsorption kinetics[26,39]. Moreover, recent studies have suggested the possibility of engineering the electronic structure of MoS_2 by varying its interlayer distance[29,34,43–46]. Kobayashi and Yamauchi reported that a 7% expansion of MoS_2 interlayers is sufficient to render it essentially with a two-dimensional single-layer model[43]. The group of Nørskov performed DFT calculation on the Mo edge of MoS_2/graphene and found $\sim$0.05 eV change of ΔG_H when the interlayer distance has a 0.37 Å discrepancy[46]. To probe the influence of expanded interlayers on their neighbouring couplings, we performed Raman study on ET&IE MoS_2 and compared that with bulk MoS_2. Figure 5a shows that the E_{2g}^1 mode of ET&IE MoS_2 increases in frequency whereas its A_{1g} mode exhibits a slight red shift. The smaller separation between the above two modes (ω_A–ω_E) for ET&IE MoS_2 indicates a weakened interlayer mechanical coupling strength, suggesting that $\sim$9.4 Å interlayer gap enables the MoS_2 to approach its single-layer equivalent and thus a modified electronic structure[45,47].

We then performed DFT calculations on non-expanded MoS_2 and interlayer-expanded MoS_2 to study the influence of the electronic structure induced by the expanded interlayer distance. Figure 5b shows that the density of states (DOS) of interlayer-expanded MoS_2 is shifted upwards as compared with that of non-expanded MoS_2, including a shift in the *d* band of $\sim$0.1 eV towards the Fermi level (Supplementary Fig. 14). This electronic effect will strengthen the H adsorption and offer an increased H coverage on the edge sites[48]. Our calculations also show that the hydrogen adsorption energy (ΔE_H) on Mo edges decreases by about 0.05 eV (a decrease of 0.01 eV on S edges, Supplementary Fig. 15 and Supplementary Note 2) for ET&IE MoS_2 as compared to that for non-expanded MoS_2 (Fig. 5c). For pristine 2H–MoS_2, previous calculations revealed that it has a ΔG_H of $+0.08$ eV at the Mo edges with only 25% H coverage under operating conditions and a strengthened H adsorption on the edge sites is needed to improve its activity[23,24]. The reduced ΔE_H ($\sim$0.05 eV) of the ET&IE MoS_2 enables an optimized bond strength of the adsorbed H on the Mo edges and thereby a faster proton adsorption kinetics[24], agreeing well with the DOS results. The advantages of edge-terminated nanostructure that exposes an abundance of active edge sites, as well as the enlarged interlayer distance with modified edge electronic structures, together lead to the high HER performance of this single MoS_2 catalyst (Fig. 5d).

Discussion

In summary, we demonstrate a new nanostructured MoS_2 catalyst with edge-terminated and interlayer-expanded features that was synthesized through a microwave heating strategy. The measured HER activity and stability of this MoS_2 structure exceed almost all the documented counterpart MoS_2 and enable the promise for exploring it as a realistic H_2 evolution electrode. Beside the edge-terminated structure that allows more active edge sites, the expanded interlayer distance can further optimize its electronic structure and therefore permits the performance gains. Our results here raise a new catalyst design concept regarding to layered materials through modulating their interlayer coupling.

Methods

Material synthesis. All chemicals were used as received without further purification. In a typical synthesis, 10 mg $(NH_4)_2MoS_4$ (99.97%, Sigma-Aldrich) was added to 6 ml DMF (anhydrous, 99.8%, Sigma-Aldrich) followed by stirring for

15 min under ambient condition. The resulting solution was transferred into a 10 ml microwave reaction vessel, which was then heated to 240 °C at the fast ramp and the temperature was maintained for 2 h in a microwave reactor (CEM corporation) operated under the sealed vessel mode. The reaction solution was cooled to room temperature with pressurized nitrogen flow and the resulting black product was collected via centrifugation (8,000 r.p.m. for 5 min). The precipitate was washed with distilled water and absolute ethanol for at least four times to remove ions and possible remnants, followed by drying at 60 °C in an oven for 4 h. For the time-dependent experiment, the temperature was set at 240 °C while reactions stopped at different times; for the temperature-dependent experiment, the reaction time was 2 h while the reaction temperatures were altered intentionally, all the corresponding products were collected for further studies.

Characterization. The as-synthesized samples were examined by X-ray powder diffraction was carried out on a Bruker D2 Phaser X-ray diffractometer with Cu Ka radiation ($\lambda = 1.5406$ Å) at 30 kV and a current of 10 mA. The morphology of the as-synthesized samples was determined by using a JEOL 2010F(s) TEM. The HRTEM observation and SAED were taken on the same machine with an acceleration voltage of 200 kV. The energy-dispersive X-ray spectra were collected with an INCA X-ray microanalysis system equipped on the JEOL 2010F(s) microscope. All samples were prepared by dropping the ethanol suspension containing uniformly dispersed nanocrystals onto the carbon-coated copper grids and dried at room temperature naturally. Raman spectra were performed using a Raman microscope (Renishaw) excited with a 514 nm excitation laser. The Fourier transform infrared (FTIR) spectra were measured on a Thermo Fisher/Nicolet 6,700 FTIR spectrometer at room temperature.

Electrocatalytic study. Electrochemical measurements were performed at room temperature using a rotating disk working electrode made of glassy carbon (PINE, 5 mm diameter, 0.196 cm^2) controlled by a CH Instruments 700C potentiostat. The glassy carbon electrode was polished to a mirror finish and thoroughly cleaned before use. Pt coil and double junction Ag/AgCl (PINE, 4 M KCl) were used as counter and reference electrodes, respectively. All the potentials reported in this work were normalized against that of the RHE.

The preparation method of the working electrodes containing investigated catalysts can be found as follows. In short, 5 mg of catalyst powder was dispersed in 1 ml of 3:1 vol/vol deionzed water/isopropanol mixed solvent, which was ultrasonicated for about 30 min to generate a homogeneous ink (no *Nafion* solution was added due to the ink can form intact and stable film on glassy carbon electrode). Then, 10 µl of the dispersion was transferred onto the glassy carbon disk, leading to the catalyst loading of 0.28 mg cm^{-2}. Finally, the as-prepared catalyst film was dried at room temperature. For comparison, bare glassy carbon electrode that has been polished and cleaned was also dried for electrochemical measurement.

Before the electrochemical measurement, the electrolyte (0.5 M H_2SO_4) was degassed by bubbling pure argon for at least 0.5 h to ensure the saturation of the electrolyte. The polarization curves were obtained by sweeping the potential from -0.35 to 0.15 V versus RHE at room temperature and 1,600 r.p.m (to remove the *in situ* formed H_2 bubbles on the RDE), with a sweep rate of 5 mV s^{-1}. The electrochemical impedance spectroscopy measurement was performed in the same configuration at overpotential of 200 mV over a frequency range from 5 MHz to 5 mHz at the amplitude of the sinusoidal voltage of 5 mV and room temperature. The MoS_2 synthesized at 240 °C for 2 h was spin coated onto FTO-coated glass slide (Sigma-Aldrich, surface resistivity $\sim 7\,\Omega$ per square; 1.5 cm × 2.5 cm; catalyst loading 22.1 µg cm^{-2}) and used as working electrode to perform chronoamperometry experiments at various overpotentials. Cyclic voltammograms performed at various sweep rates were used to estimate the C_{dl} were recorded in the potential region of 0.1–0.2 versus RHE at room temperature. The polarization curves were replotted as overpotential (η) versus log current (log j) to get Tafel plots for assessing the HER kinetics of investigated catalysts. By fitting the linear portion of the Tafel plots to the Tafel equation ($\eta = b \log(j) + a$), the Tafel slope (b) can be obtained.

DFT calculations. The hydrogen adsorption energy (ΔE_H) calculations on strip models of non-expanded MoS_2 and ET&IE MoS_2 were performed by periodic DFT using the plane wave code Vienna *Ab-initio* Simulation Package (VASP). The change in hydrogen adsorption energies is reported as $\Delta(\Delta E_H)$. Structural models are represented using the visualization tool Visualization for Electronic and STructural Analysis (VESTA). Details of the calculation and relevant references are provided in the Supplementary Note 3.

References

1. Crabtree, G. W., Dresselhaus, M. S. & Buchanan, M. V. The hydrogen economy. *Phys. Today* **57,** 39–44 (2004).
2. Walter, M. G. *et al.* Solar water splitting cells. *Chem. Rev.* **110,** 6446–6473 (2010).
3. Cook, T. R. *et al.* Solar energy supply and storage for the legacy and nonlegacy worlds. *Chem. Rev.* **110,** 6474–6502 (2010).
4. Greeley, J., Jaramillo, T. F., Bonde, J., Chorkendorff, I. B. & Norskov, J. K. Computational high-throughput screening of electrocatalytic materials for hydrogen evolution. *Nat. Mater.* **5,** 909–913 (2006).
5. Gao, M. R. *et al.* An efficient molybdenum disulfide/cobalt diselenide hybrid catalyst for electrochemical hydrogen generation. *Nat. Commun.* **6,** 5982 (2015).
6. Xu, Y. F., Gao, M. R., Zheng, Y. R., Jiang, J. & Yu, S. H. Nickel/nickel(II) oxide nanoparticles anchored onto cobalt(IV) diselenide nanobelts for the electrochemical production of hydrogen. *Angew. Chem. Int. Ed.* **52,** 8546–8550 (2013).
7. Gao, M. R., Xu, Y. F., Jiang, J. & Yu, S. H. Nanostructured metal chalcogenides: synthesis, modification, and applications in energy conversion and storage devices. *Chem. Soc. Rev.* **42,** 2986–3017 (2013).
8. Kong, D. S., Cha, J. J., Wang, H. T., Lee, H. R. & Cui, Y. First-row transition metal dichalcogenide catalysts for hydrogen evolution reaction. *Energy Environ. Sci.* **6,** 3553–3558 (2013).
9. Faber, M. S. & Jin, S. Earth-abundant inorganic electrocatalysts and their nanostructures for energy conversion applications. *Energy Environ. Sci.* **7,** 3519–3542 (2014).
10. Gao, M. R. *et al.* Mixed-solution synthesis of sea urchin-like NiSe nanofiber assemblies as economical Pt-free catalysts for electrochemical H_2 production. *J. Mater. Chem.* **22,** 13662–13668 (2012).
11. Laursen, A. B., Kegnaes, S., Dahl, S. & Chorkendorff, I. Molybdenum sulfides-efficient and viable materials for electro- and photoelectrocatalytic hydrogen evolution. *Energy Environ. Sci.* **5,** 5577–5591 (2012).
12. Morales-Guio, C. G. & Hu, X. L. Amorphous molybdenum sulfides as hydrogen evolution catalysts. *Acc. Chem. Res.* **47,** 2671–2681 (2014).
13. Benck, J. D., Hellstern, T. R., Kibsgaard, J., Chakthranont, P. & Jaramillo, T. F. Catalyzing the hydrogen evolution reaction (HER) with molybdenum sulfide nanomaterials. *ACS Catal.* **4,** 3957–3971 (2014).
14. Yan, Y., Xia, B., Xu, Z. & Wang, X. Recent development of molybdenum sulfides as advanced electrocatalysts for hydrogen evolution reaction. *ACS Catal.* **4,** 1693–1705 (2014).
15. Merki, D. & Hu, X. L. Recent developments of molybdenum and tungsten sulfides as hydrogen evolution catalysts. *Energy Environ. Sci.* **4,** 3878–3888 (2011).
16. Liao, L. *et al.* A nanoporous molybdenum carbide nanowire as an electrocatalyst for hydrogen evolution reaction. *Energy Environ. Sci.* **7,** 387–392 (2014).
17. Lu, Z. Y. *et al.* Ultrahigh hydrogen evolution performance of under-water 'superaerophobic' MoS2 nanostructured electrodes. *Adv. Mater.* **26,** 2683–2687 (2014).
18. Gopalakrishnan, D., Damien, D. & Shaijumon, M. M. MoS_2 quantum dot-interspersed exfoliated MoS_2 nanosheets. *ACS Nano* **8,** 5297–5303 (2014).
19. Chen, Z. B. *et al.* Core-shell MoO_3-MoS_2 nanowires for hydrogen evolution: a functional design for electrocatalytic materials. *Nano Lett.* **11,** 4168–4175 (2011).
20. Voiry, D. *et al.* Enhanced catalytic activity in strained chemically exfoliated WS_2 nanosheets for hydrogen evolution. *Nat. Mater.* **12,** 850–855 (2013).
21. Cheng, L. *et al.* Ultrathin WS_2 nanoflakes as a high-performance electrocatalyst for the hydrogen evolution reaction. *Angew. Chem. Int. Ed.* **53,** 7860–7863 (2014).
22. Prins, R., Debeer, V. H. J. & Somorjai, G. A. Structure and function of the catalyst and the promoter in Co-Mo hydrodesulfurization catalysts. *Catal. Rev: Sci. Eng.* **31,** 1–41 (1989).
23. Hinnemann, B. *et al.* Biornimetic hydrogen evolution: MoS_2 nanoparticles as catalyst for hydrogen evolution. *J. Am. Chem. Soc.* **127,** 5308–5309 (2005).
24. Jaramillo, T. F. *et al.* Identification of active edge sites for electrochemical H_2 evolution from MoS_2 nanocatalysts. *Science* **317,** 100–102 (2007).
25. Karunadasa, H. I. *et al.* A molecular MoS_2 edge site mimic for catalytic hydrogen generation. *Science* **335,** 698–702 (2012).
26. Bonde, J., Moses, P. G., Jaramillo, T. F., Norskov, J. K. & Chorkendorff, I. Hydrogen evolution on nano-particulate transition metal sulfides. *Faraday Discuss.* **140,** 219–231 (2008).
27. Kibsgaard, J., Chen, Z. B., Reinecke, B. N. & Jaramillo, T. F. Engineering the surface structure of MoS_2 to preferentially expose active edge sites for electrocatalysis. *Nat. Mater.* **11,** 963–969 (2012).
28. Xie, J. F. *et al.* Defect-rich MoS_2 ultrathin nanosheets with additional active edge sites for enhanced electrocatalytic hydrogen evolution. *Adv. Mater.* **25,** 5807–5813 (2013).
29. Xie, J. F. *et al.* Controllable disorder engineering in oxygen-incorporated MoS_2 ultrathin nanosheets for efficient hydrogen evolution. *J. Am. Chem. Soc.* **135,** 17881–17888 (2013).
30. Merki, D., Fierro, S., Vrubel, H. & Hu, X. L. Amorphous molybdenum sulfide films as catalysts for electrochemical hydrogen production in water. *Chem. Sci.* **2,** 1262–1267 (2011).
31. Benck, J. D., Chen, Z. B., Kuritzky, L. Y., Forman, A. J. & Jaramillo, T. F. Amorphous molybdenum sulfide catalysts for electrochemical hydrogen production: insights into the origin of their catalytic activity. *ACS Catal.* **2,** 1916–1923 (2012).

32. Lukowski, M. A. *et al.* Enhanced hydrogen evolution catalysis from chemically exfoliated metallic MoS_2 nanosheets. *J. Am. Chem. Soc.* **135,** 10274–10277 (2013).
33. Kong, D. S. *et al.* Synthesis of MoS_2 and $MoSe_2$ films with vertically aligned layers. *Nano. Lett.* **13,** 1341–1347 (2013).
34. Wang, H. T. *et al.* Electrochemical tuning of vertically aligned MoS_2 nanofilms and its application in improving hydrogen evolution reaction. *Proc. Natl Acad. Sci. USA* **110,** 19701–19706 (2013).
35. Liao, L. *et al.* MoS_2 formed on mesoporous graphene as a highly active catalyst for hydrogen evolution. *Adv. Funct. Mater.* **23,** 5326–5333 (2013).
36. Li, Y. G. *et al.* MoS_2 nanoparticles grown on graphene: an advanced catalyst for the hydrogen evolution reaction. *J. Am. Chem. Soc.* **133,** 7296–7299 (2011).
37. Wang, H. T. *et al.* Electrochemical tuning of MoS_2 nanoparticles on three-dimensional substrate for efficient hydrogen evolution. *ACS Nano* **8,** 4940–4947 (2014).
38. Youn, D. H. *et al.* Highly active and stable hydrogen evolution electrocatalysts based on molybdenum compounds on carbon nanotube-graphene hybrid support. *ACS Nano* **8,** 5164–5173 (2014).
39. Merki, D., Vrubel, H., Rovelli, L., Fierro, S. & Hu, X. L. Fe, Co, and Ni ions promote the catalytic activity of amorphous molybdenum sulfide films for hydrogen evolution. *Chem. Sci.* **3,** 2515–2525 (2012).
40. Zhu, Y. J. & Chen, F. Microwave-assisted preparation of inorganic nanostructures in liquid phase. *Chem. Rev.* **114,** 6462–6555 (2014).
41. Sun, Y. G., Wang, L., Liu, Y. Z. & Ren, Y. Birnessite-type MnO_2 nanosheets with layered structures under high pressure: elimination of crystalline stacking faults and oriented laminar assembly. *Small* **10,** 300–305 (2014).
42. Zheng, Y., Jiao, Y., Jaroniec, M. & Qiao, S. Z. Advancing the electrochemistry of the hydrogen-evolution reaction through combining experiment and theory. *Angew. Chem. Int. Ed.* **54,** 52–65 (2015).
43. Kobayashi, K. & Yamauchi, J. Electronic structure and scanning-tunneling-microscopy image of molybdenum dichalcogenide surfaces. *Phys. Rev. B* **51,** 17085–17095 (1995).
44. Zeng, Z. Y. *et al.* Single-layer semiconducting nanosheets: high-yield preparation and device fabrication. *Angew. Chem. Int. Ed.* **50,** 11093–11097 (2011).
45. Liu, K. H. *et al.* Evolution of interlayer coupling in twisted molybdenum disulfide bilayers. *Nat. Commun.* **5,** 4966 (2014).
46. Tsai, C., Abild-Pedersen, F. & Norskov, J. K. Tuning the MoS_2 edge-site activity for hydrogen evolution via support interactions. *Nano Lett.* **14,** 1381–1387 (2014).
47. Lee, C. *et al.* Anomalous lattice vibrations of single- and few-layer MoS_2. *ACS Nano* **4,** 2695–2700 (2010).
48. Hammer, B. & Norskov, J. K. Theoretical surface science and catalysis—calculations and concepts. *Adv. Catal.* **45,** 71–129 (2000).
49. Li, D. J. *et al.* Molybdenum sulfide/N-doped CNT forest hybrid catalysts for high-performance hydrogen evolution reaction. *Nano Lett.* **14,** 1228–1233 (2014).

Acknowledgements

Use of the Center for Nanoscale Materials was supported by the U.S. Department of Energy, Office of Science, Office of Basic Energy Sciences, under Contract No. DE-AC02-06CH11357.

Author contributions

Y.S. and M.-R.G. conceived the idea. M.-R.G. planned and performed the experiments, collected and analysed the data. M.K.Y.C. performed the DFT calculations and analysed the computational data. M.-R.G., M.K.Y.C. and Y.S. co-wrote the manuscript. All authors discussed the results and commented on the manuscript.

Additional information

Supplementary Information accompanies this paper at http://www.nature.com/naturecommunications

Competing financial interests: The authors declare no competing financial interests.

Reprints and permission information is available online at http://npg.nature.com/reprintsandpermissions/

How to cite this article: Gao, M.-R. *et al.* Edge-terminated molybdenum disulfide with a 9.4-Å interlayer spacing for electrochemical hydrogen production. *Nat. Commun.* 6:7493 doi: 10.1038/ncomms8493 (2015).